Academic Journal of Applied Sciences
ISSN: 3105-0549 (Print), ISSN: 3105-0557 (Online) | Vol. 2, No. 3, 2026

Tensile Elastic Response of Holed Rock Specimens under Coupled Effects of Hole Shape and Nominal Size

Xue Li

School of Energy Science and Engineering, Henan Polytechnic University, Jiaozuo, Henan, China

Abstract: To distinguish local field concentration governed by hole-boundary geometry from global compliance governed by void fraction and residual ligament, two-dimensional plane-stress models of 100 mm × 100 mm holed rock specimens were established in Abaqus. Circular, equilateral-triangular, square, and straight-walled semicircular-arched holes were considered at nominal sizes R = 20, 30, and 40 mm. The area void ratio φ and minimum lateral-ligament ratio η were introduced to quantify the geometric non-equivalence associated with different definitions of R, and the von Mises equivalent stress, displacement magnitude, and maximum in-plane principal strain were jointly analysed. The locations of high-response zones are controlled by boundary-curvature continuity and corner orientation: they occur at the lateral sidewalls of the circular hole, the two lower corners of the triangular hole, the upper corners of the square hole, and the springing regions of the arched hole. At small sizes, the response is dominated by local concentration at corners or curvature transitions; with increasing R, void fraction and ligament reduction become increasingly important. At R = 40 mm, the circular-hole model has $\varphi = 0.503$ and $\eta = 0.10$, and its peak equivalent stress, maximum displacement, and maximum principal strain reach 18.47 MPa, 6.670×10^{-1} mm, and 7.505×10^{-3}, respectively, indicating pronounced finite-boundary amplification. The triangular and square holes mainly exhibit progressively enhanced corner localization, whereas the arched hole shows weakly non-monotonic peaks but an expanding affected zone. No scale-independent ranking of hole shapes exists under the same nominal R; area void ratio and minimum ligament ratio should therefore be reported together with the nominal size. The proposed multi-field framework separating local concentration from global compliance provides a more interpretable basis for geometric design and comparison of finite holed specimens and engineering openings.

Keywords: Hole shape, nominal size, area void ratio, finite-boundary effect, elastic field.

1. Introduction

Geometric discontinuities, including natural pores, dissolution cavities, boreholes, and excavation openings, are widely present in rock masses, rock structural components, and underground engineering systems. The presence of an opening alters the load-transfer path within an otherwise continuous medium, resulting in the redistribution of stress, strain, and displacement in the vicinity of the opening boundary. Regions with high field gradients may consequently develop near corners, abrupt changes in curvature, or narrow ligaments. Previous studies have demonstrated that opening shape, opening-area ratio, and the interaction between the opening boundary and the external specimen boundary can significantly influence the deformation, strength, and crack evolution of rocks and rock-like materials [1–5,9,20]. Therefore, identifying the locations of field concentration during the elastic stage and clarifying their evolution with opening size are essential for understanding subsequent local damage tendencies and optimizing the geometric design of engineering openings.

The effect of opening shape is primarily governed by the continuity of boundary curvature and the influence of geometric corners on local load diversion. Comparative studies of circular, rectangular, triangular, and other noncircular openings have shown that smooth boundaries facilitate continuous stress transfer around the opening, whereas sharp or right-angled corners in polygonal openings are more likely to induce pronounced localization [1–5]. Experimental and numerical investigations of circular, elliptical, rectangular, and inverted-U-shaped engineering openings have further indicated that an arched roof can alleviate field gradients; nevertheless, the arch feet and the transition zones between the straight sidewalls and the curved roof remain sensitive regions for stress concentration and fracture development [9–15]. These studies provide an important basis for understanding boundary-geometry effects. However, the opening sizes, area ratios, and boundary conditions adopted in different studies are often inconsistent, thereby limiting direct comparisons across opening shapes.

In addition to local boundary geometry, opening size, orientation, and the dimensions of the remaining ligaments modify the overall load-transfer path in finite-sized specimens. Studies on specimens containing multiple openings or elliptical openings have shown that opening spacing, aspect ratio, and inclination govern the formation of stress bridges, crack-initiation locations, and crack-coalescence paths [6–8,14–16]. When circular openings coexist with joints or pre-existing cracks, the opening boundary, crack tips, and loading direction jointly determine the mixed tensile-shear response [17–20]. Variations in opening diameter also affect crack evolution around the opening, the diffraction of dynamic stress waves, and the inverse evaluation of material properties in ring-splitting tests [21–24]. Classical elasticity theory indicates that stress amplification near an opening tip is closely related to the local radius of curvature, while an ideal sharp corner may produce a stress singularity [25]. Consequently, when the same nominal parameter (R) is used to characterize openings of different shapes without simultaneously controlling the opening area, opening width, or minimum ligament dimension, the observed differences inevitably reflect a combination of opening-shape effects and finite-boundary effects.

Most existing studies have focused on strength degradation and crack propagation under compression, unloading, or dynamic loading. By contrast, systematic full-field comparisons of multiple opening shapes and nominal sizes under uniform tensile loading and linear-elastic conditions remain relatively limited. In particular, opening geometries are often ranked according to a single peak response, whereas insufficient attention has been paid to distinguishing local concentration governed by corners or abrupt curvature changes from global compliance enhancement governed by the opening fraction and remaining ligament dimensions. Such a distinction should be established on the basis of the governing equations, analytical solutions for the elastic field around openings, and the load-transfer characteristics of finite ligaments.

Accordingly, this study follows a framework comprising mechanism analysis, numerical verification, and multi-field comparison. First, theoretical relationships are established for the plane-stress elastic field, geometric concentration around the opening, and amplification induced by finite ligaments. Subsequently, twelve numerical cases are analyzed using consistent material properties, loading conditions, boundary constraints, and meshing strategies. Finally, the opening-area fraction (φ) and the minimum lateral ligament ratio (η) are introduced to jointly evaluate the equivalent stress, displacement, and maximum in-plane principal strain. On this basis, the scale-dependent mechanism governing the transition from local geometric concentration to finite-boundary-controlled behavior is clarified. Rather than pursuing a universal ranking of opening shapes independent of geometric reference criteria, this study emphasizes that the physical meaning of nominal size must be explicitly defined when conducting cross-shape comparisons.

2. Mechanism Analysis

2.1. Governing Equations of Plane-Stress Elasticity

For the two-dimensional analysis of the elastic response of thin plate-like specimens containing openings, a plane-stress assumption is adopted. In the absence of body forces, the stress field within the domain must satisfy the static equilibrium equations:

$$\begin{cases} \frac{\partial\sigma_x}{\partial x}+\frac{\partial\tau_{xy}}{\partial y}=0, \\ \frac{\partial\tau_{xy}}{\partial x}+\frac{\partial\sigma_y}{\partial y}=0. \end{cases} \tag{1}$$

The displacement components (u_x) and (u_y) are related to the small-strain components through the following kinematic relations:

$$\begin{cases} \varepsilon_x=\frac{\partial u_x}{\partial x}, \quad \varepsilon_y=\frac{\partial u_y}{\partial y}, \\ \gamma_{xy}=\frac{\partial u_x}{\partial y}+\frac{\partial u_y}{\partial x}. \end{cases} \tag{2}$$

For a homogeneous, isotropic, and linearly elastic material, the constitutive relationship under plane-stress conditions is expressed as:

$$\begin{gathered} \sigma_x=\frac{E}{1-\nu^2}\left(\varepsilon_x+\nu\varepsilon_y\right), \\ \sigma_y=\frac{E}{1-\nu^2}\left(\nu\varepsilon_x+\varepsilon_y\right), \\ \tau_{xy}=\frac{E}{2(1+\nu)}\gamma_{xy}. \end{gathered} \tag{3}$$

Where (E) denotes Young's modulus and (ν) denotes Poisson's ratio. Equations (1)–(3) collectively govern the redistribution of the elastic field induced by the opening. Specifically, the opening boundary modifies the boundary conditions, geometric discontinuities alter the local stress gradients, and the remaining ligaments determine the effective cross-sectional area available for load redistribution.

2.2. Nominal Size and Finite-Ligament Amplification

To distinguish the effects of opening-boundary geometry from the reduction in the effective load-bearing cross section, the nominal relative size (λ), opening-area fraction (φ), and minimum lateral ligament ratio (η) are defined as follows:

$$\begin{gathered} \lambda=\frac{R}{W}, \qquad \varphi=\frac{A_h}{W^2}, \\ \eta=\frac{l_{min}}{W}=\frac{W-b_h}{2W}. \end{gathered} \tag{4}$$

Where (W) is the specimen width, (A_h) is the opening area, (b_h) is the transverse width of the opening, and (l_{min}) is the minimum horizontal ligament between the opening boundary and either lateral boundary of the specimen. According to the definition of (R) adopted in this study, the dimensionless geometric relationships for the four opening shapes can be expressed as follows:

$$\begin{gathered} \varphi_c=\pi\lambda^2, \qquad \varphi_t=\frac{\sqrt{3}}{4}\lambda^2, \\ \varphi_s=\lambda^2, \qquad \varphi_a=\left(\frac{1}{2}+\frac{\pi}{8}\right)\lambda^2. \end{gathered} \tag{5}$$

Based on the transverse opening width, the minimum lateral ligament ratio for each opening shape is obtained as follows:

$$\begin{gathered} \eta_c=\frac{1-2\lambda}{2}, \\ \eta_t=\eta_s=\eta_a=\frac{1-\lambda}{2}. \end{gathered} \tag{6}$$

For the horizontal cross section passing through the opening center, if local bending around the opening is neglected and the resultant external load is assumed to be jointly carried by the two lateral ligaments, the average axial stress in the ligaments can be estimated as:

$$\bar{\sigma}_{lig}\approx\frac{\sigma_0 W}{W-b_h}=\frac{\sigma_0}{2\eta} \tag{7}$$

Equation (7) reveals the fundamental origin of finite-boundary amplification: as (η) decreases, the nominal average stress acting on the remaining load-bearing cross section increases. For the circular opening, (b_h=2R), and therefore (η) decreases with (λ) at twice the rate observed for the other opening shapes. When (R=40mm), (η=0.10), and the average ligament stress predicted by Eq. (7) reaches approximately ($5\sigma_0$). Under this condition, the local curvature effect becomes strongly coupled with the overall reduction in the load-bearing cross section.

3. Numerical Simulation

3.1. Geometric Model and Comparative Parameters

A two-dimensional plane-stress finite-element model of a specimen containing a centrally located opening was established using Abaqus. The specimen width and height were both set to (W=100mm), and the center of the opening coincided with the geometric center of the specimen. Four opening geometries were considered: circular, equilateral triangular, square, and semicircular-arched openings with vertical sidewalls. The nominal characteristic size (R) was set to 20, 30, and 40 mm, corresponding to nominal relative sizes (λ=R/W) of 0.20, 0.30, and 0.40, respectively. A total of 12 numerical cases were therefore analyzed.

For the circular opening, (R) denotes the radius, whereas for the equilateral triangular and square openings, (R) denotes the side length. For the semicircular-arched opening with vertical sidewalls, both the overall height and overall width were defined as (R), while the crown radius and straight-sidewall height were each equal to (R/2). The opening orientation, material properties, loading configuration, and mesh-control criteria were kept consistent across all cases. A schematic illustration of the numerical models is presented in Fig. 1, and the principal computational parameters are summarized in Table 1.

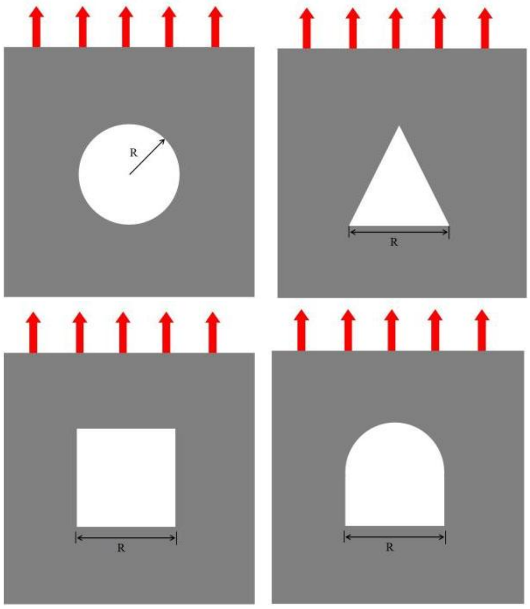

Figure 1. Schematic finite-element models of specimens containing central openings of different shapes

Table 1. Finite-element model configuration and principal computational parameters

Item	Specification
Specimen geometry and opening arrangement	100 mm×100 mm; one centrally located opening
Opening shape	Circular, equilateral triangular, square, and semicircular-arched opening with vertical sidewalls
Nominal characteristic size, (R)	20, 30, 40 mm
Material model	Homogeneous, isotropic, and linearly elastic
Elastic parameters	E=2.5 GPa, ν=0.25
Loading condition	A uniformly distributed normal tensile stress of 1 MPa applied to the top boundary
Boundary conditions	(u_x=u_y=0) along the bottom boundary; the left and right boundaries are traction-free

To explicitly characterize the geometric nonequivalence arising from the different definitions of (R), the opening-area fraction (φ=A_h/W^2) and the minimum lateral ligament ratio (η=l_min/W) are introduced, where (A_h) is the opening area and (l_min}) is the minimum horizontal ligament width between the opening boundary and the lateral edge of the specimen. Table 2 summarizes the opening width, area coefficient, (φ), and (η) for the four opening geometries. It can be observed that, for the same (R), the actual width of the circular opening is twice that of the other opening shapes. Moreover, (φ) increases more rapidly and (η) decreases more markedly for the circular opening. Therefore, comparisons across different opening shapes should be interpreted as coupled responses involving opening-boundary geometry, opening-area fraction, and finite-boundary effects.

Table 2. Dimensionless geometric parameters of openings with different shapes

Opening shape	Opening width b/R	Area coefficient A_h/R^2	φ	η
Circular opening	2	π	0.126/0.283/0.503	0.30/0.20/0.10
Equilateral triangular opening	1	√3/4	0.017/0.039/0.069	0.40/0.35/0.30
Square opening	1	1	0.040/0.090/0.160	0.40/0.35/0.30
Semicircular-arched opening with vertical sidewalls	1	1/2+π/8	0.036/0.080/0.143	0.40/0.35/0.30

3.2. Material Properties, Boundary Conditions, and Mesh Discretization

To highlight the influence of opening geometry on the distribution of the elastic field, the material was modeled as homogeneous, isotropic, and linearly elastic, with a Young's modulus of (E=2.5GPa) and a Poisson's ratio of (ν=0.25). This parameter set was adopted to construct an idealized equivalent rock model and does not represent any specific lithology. Plasticity, damage, and fracture evolution were not considered in the model. Therefore, the numerical results characterize only the redistribution of the elastic field under the prescribed loading level and are not intended for direct prediction of crack paths or ultimate load-bearing capacity.

A uniformly distributed upward normal tensile stress of (1MPa) was applied to the top boundary of the specimen and was denoted as the nominal applied stress (σ_0). The bottom boundary was fully constrained by imposing (u_x=u_y=0), whereas the left and right boundaries were traction-free. The use of identical boundary conditions ensured relative comparability among the numerical cases. However, the fully fixed bottom boundary introduces local constraint effects and suppresses lateral deformation near the specimen end. Accordingly, the present study focuses on relative responses within the same modeling framework, and the results are not extrapolated to represent the solutions for an infinite plate or a standard uniaxial tensile test.

The models were discretized using eight-node quadratic plane-stress quadrilateral elements with reduced integration (CPS8R). The mesh was refined in the vicinity of the opening and gradually coarsened toward the far-field region. The same element type and mesh-control strategy were adopted for all numerical cases. Curved boundaries were approximated using quadratic elements, whereas the equilateral triangular and square openings were modeled with ideal sharp corners. Consequently, the local peak values at these corners may vary with mesh size, result extrapolation, and nodal averaging procedures. Comparisons involving sharp-cornered openings therefore consider not only the peak values but also the extent of the high-response regions and the gradients of the contour lines. A single-node extreme value is not regarded as an intrinsic material parameter.

3.3. Output Variables and Evaluation Metrics

The Abaqus output variables S, Mises, U, Magnitude, and E, Max. In-Plane Principal were extracted during post-processing to characterize the von Mises equivalent stress (σ_{eq}), displacement magnitude (U), and maximum in-plane principal strain ($\varepsilon_{1,\ max}$), respectively. Under plane-stress conditions, the von Mises equivalent stress is expressed as:

$$\sigma_{eq}=\sqrt{\sigma_x^2-\sigma_x\sigma_y+\sigma_y^2+3\tau_{xy}^2} \tag{8}$$

The displacement magnitude is obtained from the displacement components as:

$$U=\sqrt{u_x^2+u_y^2} \tag{9}$$

When the engineering shear strain is adopted, the maximum in-plane principal strain is given by:

$$\varepsilon_{1,max}=\frac{\varepsilon_x+\varepsilon_y}{2}+\sqrt{\left(\frac{\varepsilon_x-\varepsilon_y}{2}\right)^2+\left(\frac{\gamma_{xy}}{2}\right)^2} \tag{10}$$

To quantify the local stress amplification around the opening, an equivalent-stress amplification factor (K_eq) is defined as:

$$K_{eq}=\frac{\sigma_{eq,max}}{\sigma_0} \tag{11}$$

Taking the elongation (U_0) of an unperforated one-dimensional elastic bar subjected to the same nominal stress as the reference, the nominal compliance amplification factor (K_U) is defined as:

$$U_0=\frac{\sigma_0 H}{E},\quad K_U=\frac{U_{max}}{U_0}=\frac{E\,U_{max}}{\sigma_0 H}. \tag{12}$$

Where (H) denotes the specimen height. (K_eq) is used to compare the local multiaxial stress amplification around the opening. It is neither equivalent to the classical stress concentration factor defined using a normal stress component in a specified direction nor employed as a failure criterion for brittle rock. (K_U) is used to characterize the increase in the overall structural compliance induced by the opening.

For contour comparisons among different cases, the peak value indicated by the legend, contour-line density, extent of the high-response region, and its tendency to connect with the external boundaries were considered simultaneously. This approach avoids drawing conclusions solely from the apparent area of a given contour color or from a single-node extreme value at an ideal sharp corner.

4. Results and Analysis

4.1. Equivalent Stress Field: Local Concentration and Finite-Boundary Amplification

Figure 2 presents the von Mises equivalent stress contours for the four opening shapes at (R=20), 30, and 40 mm. In all cases, the stress fields are approximately symmetric about the vertical centerline. Relatively low-stress bands develop above and below the openings and extend along the loading direction, whereas high-gradient regions occur near the lateral sides of the opening boundaries, geometric corners, or arch springings. As (R) increases, the disturbed region around the opening gradually evolves from a locally confined zone toward the lateral specimen boundaries, indicating an increasingly pronounced interaction between opening-geometry-controlled local concentration and the finite boundaries of the specimen.

For the circular opening, the high-stress regions are consistently located at the two ends of the horizontal diameter, and the peak equivalent stress increases from 3.585 MPa to 6.699 and 18.47 MPa as (R) increases. At (R=40mm), the opening diameter reaches 80 mm, leaving a lateral ligament of only 10 mm on each side. The high-stress band nearly connects the opening boundary with the specimen edge, indicating that thin-ligament control has become more influential than the mitigating effect associated with continuous boundary curvature. For the triangular opening, localization occurs primarily at the two lower corners and along the adjacent inclined edges, with the peak stress increasing from 4.298 MPa to 5.196 and 6.229 MPa. For the square opening, the response is mainly governed by the upper corners and vertical sidewalls, and the corresponding peak values increase from 3.020 MPa to 3.917 and 5.235 MPa. Both polygonal openings exhibit an increase in corner-related peak stress and an expansion of the high-stress region along the opening boundary; however, their far-field disturbance remains weaker than that observed for the large circular opening. For the arched opening, the semicircular crown promotes a relatively smooth load-transfer path, while high-gradient regions consistently develop at the arch springings and at the transitions between the vertical sidewalls and the curved roof. The peak stresses are 3.482, 3.236, and 3.719 MPa, respectively. Although these values show a weakly non-monotonic variation, the width of the high-response band continues to increase with (R).

The ranking of peak equivalent stress at the same nominal (R) varies with scale. At (R=20mm), the ranking is triangular opening (>) circular opening (>) arched opening (>) square opening. At (R=30) and 40 mm, it changes to circular opening (>) triangular opening (>) square opening (>) arched opening. In conjunction with Table 2, these results indicate that, at small scales, the minimum ligaments remain relatively wide and the response is governed primarily by corner sharpness and abrupt boundary transitions. At intermediate and large scales, however, the opening-area fraction of the circular opening increases rapidly and its minimum ligament ratio decreases markedly, causing finite-boundary amplification to become the dominant mechanism.

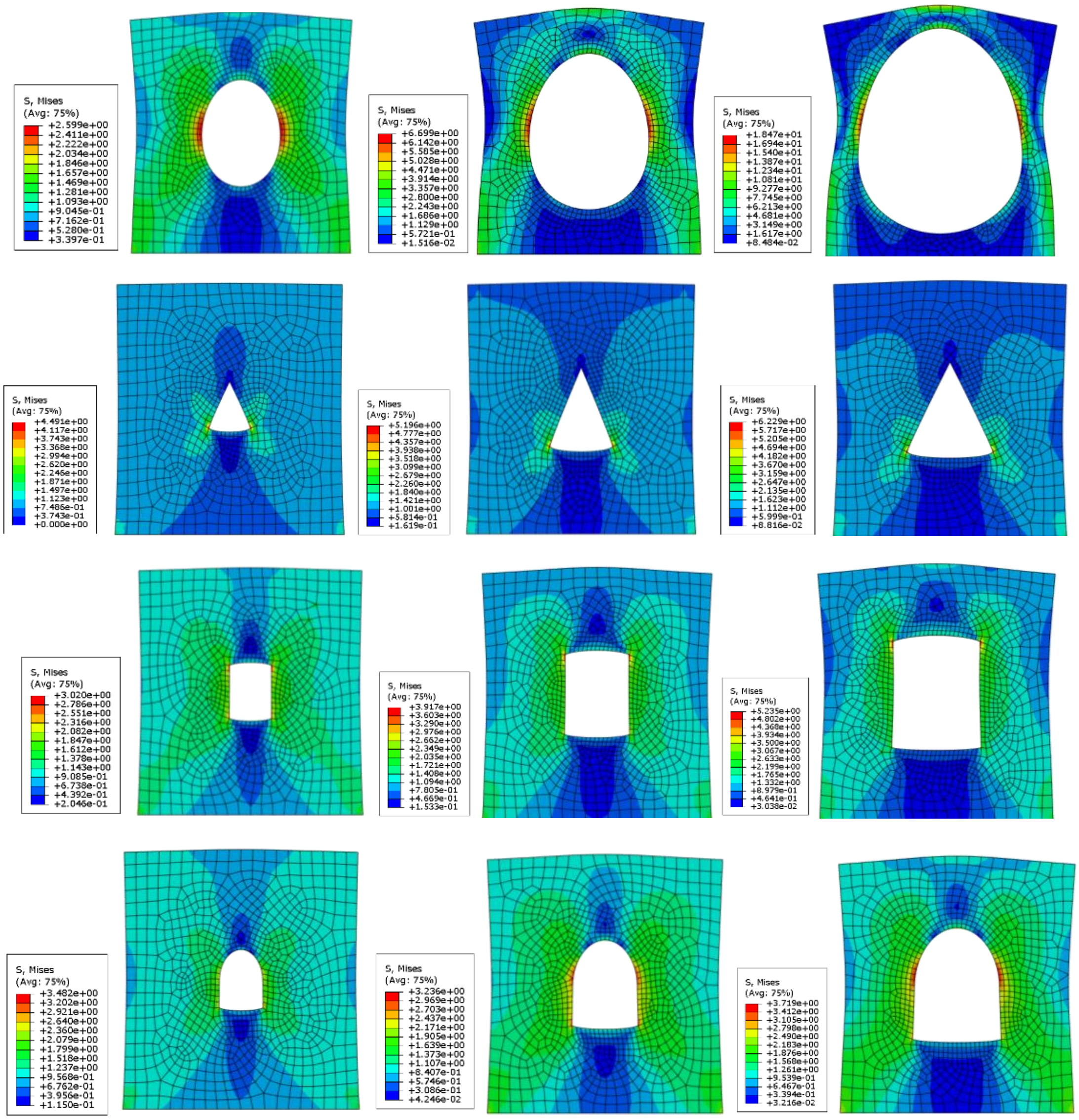

Figure 2. Contours of von Mises equivalent stress for different opening shapes and nominal sizes

4.2. Displacement Field: Global Compliance and Local Deformation Compatibility

As shown in Fig. 3, the displacement magnitude generally increases from the fixed bottom boundary toward the tensile-loaded top boundary, where a continuous high-displacement band develops. The opening affects the displacement field in two ways. First, it causes the iso-displacement contours near the opening boundary to bend, become compressed, or bifurcate, reflecting the local compatibility of deformation. Second, it reduces the effective load-bearing cross section and thereby alters the overall compliance of the specimen. Accordingly, interpretation of the displacement contours should consider both the maximum displacement and the morphology of the iso-displacement contours around the opening.

For the circular opening, the iso-displacement contours remain continuous as they pass around the opening boundary. However, as (R) increases, the lateral ligaments become rapidly thinner, and the maximum displacement increases from (4.596×10^{-2}mm) to (1.558×10^{-1}) and (6.670×10^{-1}mm). At (R=40mm), the high-displacement region near the top boundary expands markedly, indicating pronounced global softening. For the triangular opening, local turning of the contours occurs mainly near the sharp corners, while the maximum displacement increases only from (4.792×10^{-2}mm) to (5.645×10^{-2}mm), indicating that its scale-dependent response remains largely confined to the corner regions. For the square opening, the contours become densely distributed near the upper corners and vertical sidewalls, and the maximum displacement increases to (8.395×10^{-2}mm). For the arched opening, local contour deflection occurs near the arch springings and along the vertical sidewalls, and the maximum displacement increases to (7.368×10^{-2}mm). Compared with the square opening, deformation transfer across the curved crown of the arched opening is smoother.

As (R) increases from 20 to 40 mm, the maximum displacements of the circular, triangular, square, and arched openings increase by factors of approximately 14.51, 1.18, 1.75, and 1.58, respectively. After normalization using Eq. (16), the corresponding (K_U) values at (R=20/30/40mm) are 1.15/3.90/16.68 for the circular opening, 1.20/1.23/1.41 for the triangular opening, 1.20/1.63/2.10 for the square opening, and 1.17/1.42/1.84 for the arched opening. These differences indicate that the scale sensitivity of the maximum displacement and (K_U) is governed primarily by the opening-area fraction and remaining ligament dimensions. By contrast, abrupt turning of the iso-displacement contours near the opening boundary mainly reflects local deformation incompatibility induced by sharp corners or abrupt changes in curvature. Although the triangular opening exhibits pronounced corner-related gradients, it produces the lowest overall compliance.

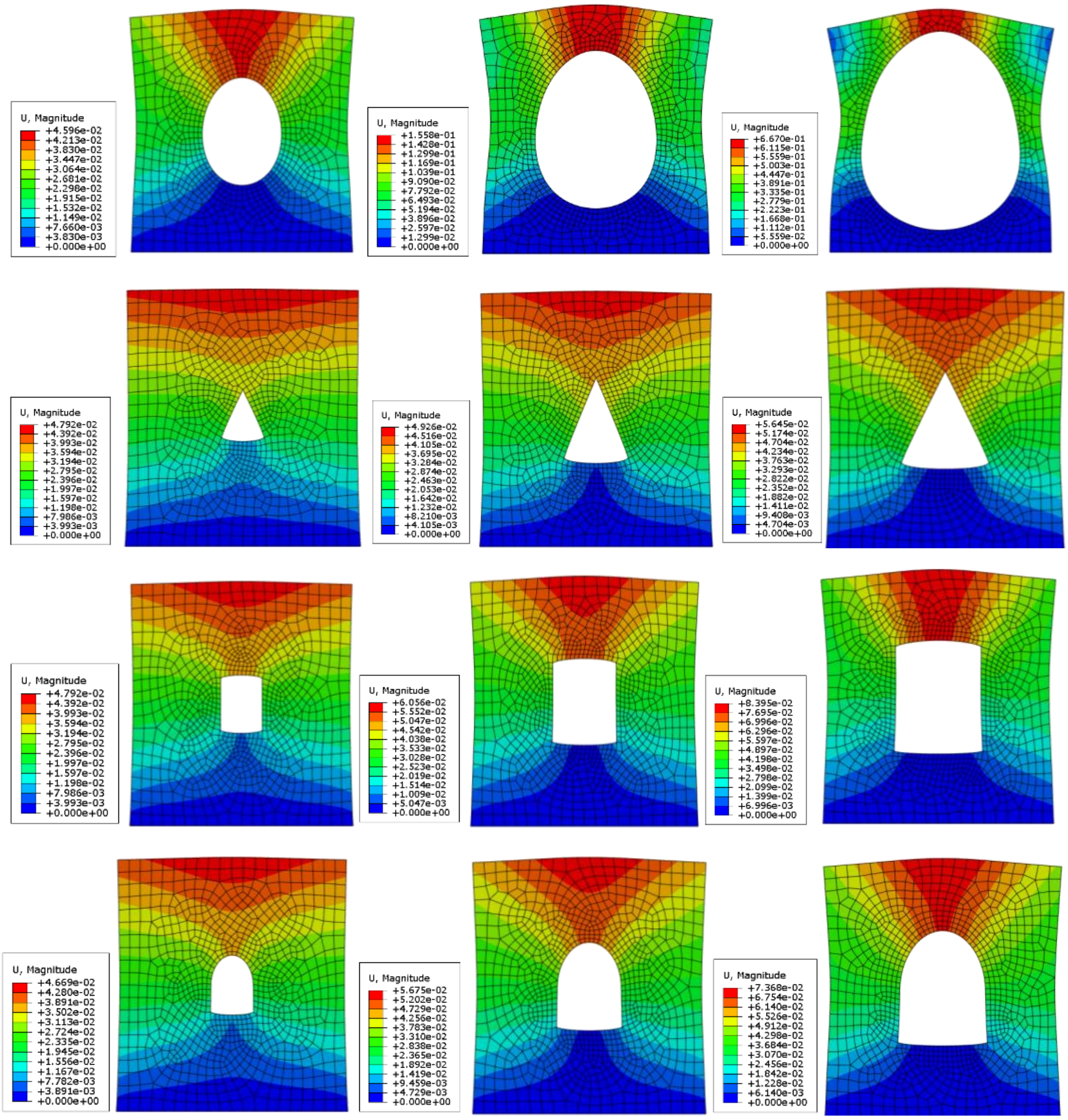

Figure 3. Contours of displacement magnitude for different opening shapes and nominal sizes

4.3. Principal Strain Field: Tensile Localization and Its Scale-Dependent Evolution

As shown in Fig. 4, the primary concentration regions in the maximum in-plane principal strain field are generally consistent with those observed in the equivalent stress field, although the principal strain field is more sensitive to the tensile direction and the orientation of the opening boundary. In all cases, regions of high positive principal strain develop near the lateral sides of the opening boundary, geometric corners, or arch springings. Under the linear-elastic assumption, these regions represent potential locations of elastic tensile localization and should not be directly interpreted as actual crack or damage zones.

For the circular opening, the peak principal strain increases from (1.052×10^{-3}) to (2.682×10^{-3}) and (7.505×10^{-3}). At (R=40mm), the high-strain band extends across most of the lateral ligaments, indicating that the local strain around the opening boundary and the overall tensile deformation of the remaining cross section increase simultaneously. For the triangular opening, the high principal strain is concentrated at the two lower corners and extends along the inclined edges in a wing-like pattern, with the peak value increasing from (1.624×10^{-3}) to (2.536×10^{-3}). For the square opening, the dominant response gradually changes from localization at the upper corners to combined control by the corners and vertical sidewalls, while the peak strain increases from (1.238×10^{-3}) to (2.154×10^{-3}). For the arched opening, the peak strain exhibits a weakly non-monotonic variation within the range of (1.315×10^{-3})–(1.492×10^{-3}), whereas the high-strain bands near the arch springings continue to expand with increasing (R).

At (R=20mm), the peak principal strain follows the order triangular opening (>) arched opening (>) square opening (>) circular opening. At (R=30) and 40 mm, the ranking changes to circular opening (>) triangular opening (>) square opening (>) arched opening. This transition is consistent with that observed in the equivalent stress field, further demonstrating that the small-scale response is governed mainly by sharp corners and local boundary transitions, whereas the large-scale response is jointly controlled by the opening-area fraction, minimum ligament dimensions, and boundary curvature. Compared with the equivalent stress, the maximum principal strain provides a more direct representation of tensile deformation localization and can therefore serve as an important complementary indicator for identifying potentially sensitive regions.

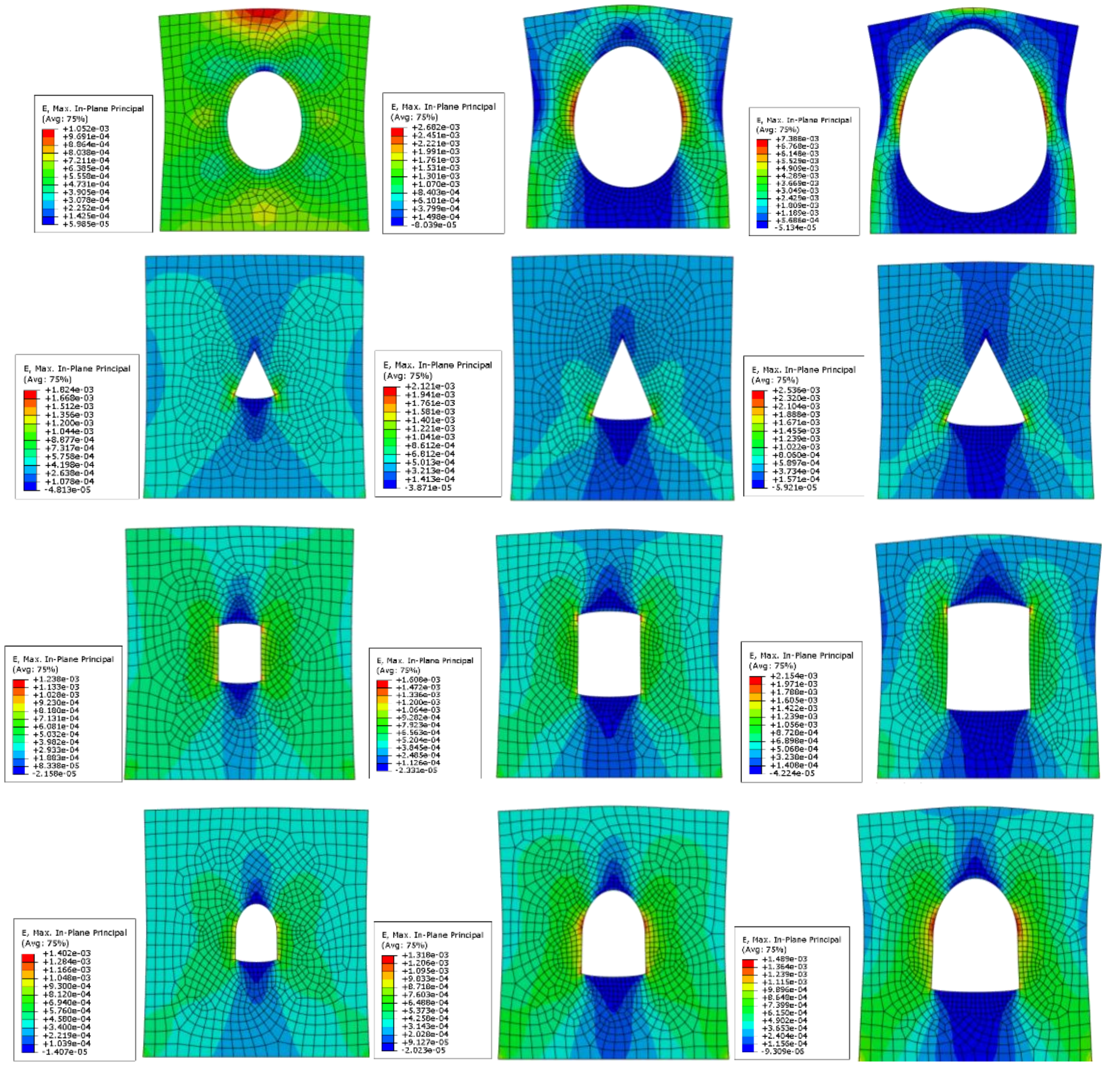

Figure 4. Contours of the maximum in-plane principal strain for different opening shapes and nominal sizes

4.4. Peak-Response Metrics and the Coupled Mechanism of Local Concentration and Global Softening

Table 3 summarizes the peak values extracted from the legends of Figs. 2–4, together with the dominant high-response regions for each opening shape. These data are used to compare the scale-dependent evolution of local stress–strain concentration and global structural compliance.

Table 3. Peak responses and dominant high-response regions for different opening shapes (R=20/30/40mm)

Opening shape	$\sigma_{eq,max}$/MPa	Umax/mm	$\varepsilon_{1,max}$	Dominant high-response region
Circular opening	3.585 6.699 18.47	4.596E-2 1.558E-1 6.670E-1	1.052E-3 2.682E-3 7.505E-3	Lateral sides of the opening boundary
Equilateral triangular opening	4.298 5.196 6.229	4.792E-2 4.920E-2 5.645E-2	1.624E-3 2.121E-3 2.536E-3	Two lower corners and adjacent inclined edges
Square opening	3.020 3.917 5.235	4.792E-2 6.505E-2 8.395E-2	1.238E-3 1.608E-3 2.154E-3	Upper corners and vertical sidewalls
Semicircular-arched opening with vertical sidewalls	3.482 3.236 3.719	4.669E-2 5.675E-2 7.368E-2	1.492E-3 1.315E-3 1.405E-3	Arch springings and vertical-sidewall–arc transition regions

Note: The three values in each group correspond sequentially to R=20, 30, and 40 mm. The peak values at sharp corners depend on the mesh and post-processing procedure.

Because (σ_0=1MPa), the equivalent-stress amplification factor (Keq) defined by Eq. (11) is numerically equal to ($\sigma_{eq,max}$). For the circular opening, (K_eq) increases sharply from 6.699 to 18.47 at (R=40mm). The values for the triangular and square openings increase steadily with (R), whereas those for the arched opening fluctuate slightly within the range of 3.236–3.719. Meanwhile, the (K_U) value of the circular opening, calculated using Eq. (12), increases from 1.15 to 16.68, whereas (K_U) remains below 2.10 for all other opening shapes at (R=4mm). In conjunction with (η) and (φ) in Table 2 and Eq. (7), these results demonstrate that the variation in peak response is not governed solely by opening sharpness. Rather, it results from the combined effects of local boundary geometry, increased average stress in the remaining ligaments, and reduced overall effective stiffness.

The coupled multi-field responses can be classified into two general mechanisms. For the circular opening, the equivalent stress, displacement, and principal strain increase simultaneously and markedly, indicating coupling between thin-ligament-induced local concentration and global softening. The triangular opening is characterized primarily by enhanced stress–strain localization at the corners, while its overall displacement changes only slightly. For the square opening, the three peak-response quantities increase in an approximately synchronous manner. For the arched opening, the overall displacement increases continuously, whereas the local stress and strain peaks remain relatively stable. This classification provides a more effective explanation of the changing dominant response mechanisms at different scales than a ranking based solely on the peak values associated with each opening shape.

The high equivalent-stress and principal-strain regions are governed by the lateral sides of the circular opening, the lower corners of the triangular opening, the upper corners of the square opening, and the arch springings of the arched opening, whereas the maximum displacement generally occurs along the tensile-loaded top boundary. Accordingly, the equivalent stress and principal strain are used to identify local concentration, while displacement is used to evaluate global compliance. For openings with sharp corners, the response should be assessed by jointly considering the peak value, the extent of the high-response region, the variation along paths surrounding the opening, and the tendency of the high-value bands to connect with the external boundaries. This approach avoids treating a mesh-dependent single-node extreme value as an intrinsic material parameter.

5. Discussion

5.1. Controlling Mechanisms of Local Boundary Geometry

The presence of an opening forces the axial load to bypass the traction-free boundary and to be redistributed through the lateral ligaments. In essence, this process reflects the modification of the elastic boundary-value problem governed by Eqs. (1)–(3) through the traction-free opening-boundary condition given in Eq. (4). For the circular opening, the boundary normal varies continuously, allowing the field variables to change direction smoothly along the opening boundary. The high-response regions located at the left and right sides of the circular opening are consistent with the analytical solution described by Eq. (5). In contrast, the boundary normal is discontinuous at the corners of the triangular and square openings, causing pronounced contour compression in the vicinity of the corners, in agreement with the singular asymptotic characteristics represented by Eq. (7). For the arched opening, the crown consists of a smooth circular arc, whereas the arch springings define the transition from the straight sidewalls to the curved boundary. The increased local rate of change in the boundary normal therefore produces persistent high-response regions at these transition zones. These observations are consistent with the boundary-geometry effects reported in previous studies of openings with different shapes, inverted-U-shaped openings, and elliptical openings [1–5, 9–15].

The location of local concentration is not determined solely by corner sharpness; it is also influenced by opening orientation, the alignment of straight boundaries, and the imposed boundary constraints. In the present model, the apex of the triangular opening points upward, whereas the dominant high-response regions occur at the two lower corners. For the square opening, the two upper corners exhibit more pronounced responses. These results demonstrate that the relative orientation between the corners and the principal tensile direction is also an important controlling factor. Ideal sharp corners are singular in continuum elastic solutions [25], and finite-element peak values therefore depend on mesh resolution, result extrapolation, and nodal averaging procedures. Accordingly, engineering design and numerical comparison should preferably employ finite corner radii or chamfers, while the response distribution and affected region around the opening should be given greater emphasis than single-node extreme values.

5.2. Scale Transition from Local Concentration to Finite-Boundary Control

Different definitions of (R) were adopted for the four opening shapes; therefore, the same value of (R) does not correspond to either equal opening area or equal opening width. According to Eqs. (9) and (10), the area coefficients of the circular, square, equilateral triangular, and arched openings are (π, 1, $\sqrt{3}$, $\sqrt{4}$), and ($1/2+\pi/8$), respectively. In addition, (η) decreases most rapidly with increasing (λ) for the circular opening. At (R=40mm), the opening-area fraction of the circular opening reaches 0.503 and the minimum lateral ligament ratio decreases to 0.10, whereas (η) remains 0.30 for all other opening shapes. Based on Eq. (11), the average ligament stress across the central section of the circular-opening specimen is estimated to be approximately ($5\sigma_0$), compared with approximately ($1.67\sigma_0$) for the other opening geometries. This difference explains the simultaneous sharp increases in stress, displacement, and principal strain observed for the large circular opening. It also demonstrates that this response cannot be attributed simply to the circular opening being inherently more critical.

As (R) increases, the relative contributions of local and global effects change progressively. The triangular and square openings are characterized mainly by expansion of the corner-dominated high-response regions. The arched opening exhibits an enlarged zone of influence while maintaining relatively stable peak values. By contrast, the circular opening rapidly enters a thin-ligament-controlled regime. Rather than ranking the opening shapes solely according to their peak responses, the present study jointly considers the opening-area fraction (φ), minimum ligament ratio (η), and three field variables. This approach enables the effects of local geometric concentration to be distinguished from those of global cross-sectional weakening and constitutes a principal advantage of the proposed analytical framework. Future studies should separately adopt equal-area or equal-porosity configurations and equal-minimum-ligament or equal-opening-width configurations to further isolate the respective contributions of boundary curvature, corner geometry, and reduction of the effective load-bearing cross section [8, 21–24].

5.3. Engineering Implications and Scope of Applicability

The von Mises equivalent stress is suitable for comparing local multiaxial stress levels. However, rock materials exhibit pronounced tensile–compressive asymmetry, and actual tensile crack initiation is more directly related to the maximum principal tensile stress, principal strain, and defect evolution. Therefore, (K_eq) should be interpreted as an equivalent-stress amplification metric under a unified loading and modeling framework. It should not be treated as equivalent to a classical normal-stress concentration factor or as a direct failure criterion for rock. Potential tensile-sensitive regions should instead be evaluated by combining the maximum principal stress, principal strain, and subsequent damage analysis.

From an engineering perspective, ideal sharp corners should be avoided, the corner radius should be increased, and the transition geometry at the arch springings should be optimized. For large openings, particular attention should also be paid to controlling the minimum remaining ligament and reinforcing structurally weak regions. The present study adopts a homogeneous, isotropic, and linearly elastic model, a fully fixed bottom boundary, and opening geometries that are not area-equivalent. Rock heterogeneity, damage and crack propagation, finite corner radii, and systematic mesh-convergence analysis were not considered. These simplifications facilitate clear identification of the underlying geometric mechanisms but limit the direct engineering extrapolation of the results.

Accordingly, the conclusions of this study are applicable primarily to relative comparisons of elastic-field responses within a unified modeling framework. Before the results are used to predict failure loads or crack trajectories, further validation is required through equal-area and equal-ligament models, mesh-convergence studies, path-based evaluation around the openings, nonlinear constitutive modeling, and physical tensile tests.

6. Conclusions

(1) The geometry of the opening boundary determines the dominant locations of the local high-response regions. For the circular opening, these regions occur at the left and right sidewalls; for the triangular opening, at the two lower corners and adjacent inclined edges; for the square opening, at the upper corners and vertical sidewalls; and for the arched opening, at the arch springings and the transitions between the vertical sidewalls and the circular arc. The high-value regions of equivalent stress and maximum principal strain generally coincide, whereas the displacement field reflects both local deformation compatibility and global structural compliance.

(2) Specimens containing openings exhibit a scale-dependent transition from boundary-geometry-induced concentration to finite-ligament control. At small scales, the curvature and corner effects represented by Eqs. (5)–(7) govern the local field gradients. As (R) increases, the increase in opening-area fraction and reduction in minimum ligament dimension described by Eqs. (9) and (10) progressively become dominant. Consequently, no scale-independent ranking of opening shapes can be established at the same nominal (R).

(3) As (R) increases from 20 to 40 mm, the peak equivalent stress, maximum displacement, and maximum principal strain of the circular-opening specimen increase from 3.585MPa, (4.596×10-2mm), and (1.052×10-3mm) to 18.47MPa, (6.670×10-1mm), and (7.505×10-3), respectively. The triangular and square openings are characterized primarily by a continuous intensification of corner-induced localization, whereas the arched opening exhibits weakly non-monotonic variations in peak response accompanied by an expansion of the affected region.

(4) Comparisons among different opening shapes should simultaneously report the nominal size, opening-area fraction, and minimum ligament ratio, while distinguishing local concentration metrics from global compliance metrics. The proposed multi-field framework of "local concentration–global softening" improves the interpretability of comparisons among geometrically nonequivalent openings. However, peak values at ideal sharp corners are mesh-dependent, and the present results should not be directly extrapolated to predict the failure load or crack trajectory of actual rock masses.

References

[1] Gui, Y. L., Zhao, Z. Y., Zhang, C., et al. (2017). Numerical investigation of the opening effect on the mechanical behaviours in rocks under uniaxial loading using hybrid continuum-discrete element method. Computers and Geotechnics, 90, 55-72. https://doi.org/10.1016/j.compgeo.2017.05.021

[2] Chen, S. J., Xia, Z. G., Feng, F., et al. (2021). Numerical study on strength and failure characteristics of rock samples with different hole defects. Bulletin of Engineering Geology and the Environment, 80, 1523-1540. https://doi.org/10.1007/s10064-020-01964-y

[3] Wu, H., Zhao, G. Y., & Liang, W. Z. (2020). Mechanical properties and fracture characteristics of pre-holed rocks subjected to uniaxial loading: A comparative analysis of five hole shapes. Theoretical and Applied Fracture Mechanics, 105, 102433. https://doi.org/10.1016/j.tafmec.2019.102433

[4] Li, D. Y., Zhu, Q. Q., Zhou, Z. L., et al. (2017). Fracture analysis of marble specimens with a hole under uniaxial compression by digital image correlation. Engineering Fracture Mechanics, 183, 109-124. https://doi.org/10.1016/j.engfracmech.2017.05.035

[5] Feng, F., Chen, S. J., Li, D. Y., et al. (2019). Analysis of fractures of a hard rock specimen via unloading of central hole with different sectional shapes. Energy Science & Engineering, 7(6), 2265-2286. https://doi.org/10.1002/ese3.432

[6] Wong, R. H. C., & Lin, P. (2015). Numerical study of stress distribution and crack coalescence mechanisms of a solid containing multiple holes. International Journal of Rock Mechanics and Mining Sciences, 79, 41-54. https://doi.org/10.1016/j.ijrmms.2015.08.003

[7] Lin, P., Wong, R. H. C., & Tang, C. A. (2015). Experimental study of coalescence mechanisms and failure under uniaxial compression of granite containing multiple holes. International Journal of Rock Mechanics and Mining Sciences, 77, 313-327. https://doi.org/10.1016/j.ijrmms.2015.04.017

[8] Bai, Q. S., Tu, S. H., & Zhang, C. (2016). DEM investigation of the fracture mechanism of rock disc containing hole(s) and its influence on tensile strength. Theoretical and Applied Fracture Mechanics, 86, 197-216. https://doi.org/10.1016/j.tafmec.2016.07.005

[9] Cai, X., Yuan, J. F., Zhou, Z. L., et al. (2023). Effects of hole shape on mechanical behavior and fracturing mechanism of rock: Implications for instability of underground openings. Tunnelling and Underground Space Technology, 141, 105361. https://doi.org/10.1016/j.tust.2023.105361

[10] Zhong, Z. B., Deng, R. G., Lv, L., et al. (2018). Fracture mechanism of naturally cracked rock around an inverted U-shaped opening in a biaxial compression test. International Journal of Rock Mechanics and Mining Sciences, 103, 242-253. https://doi.org/10.1016/j.ijrmms.2018.01.047

[11] Wu, H., Kulatilake, P. H. S. W., Zhao, G. Y., et al. (2019). A comprehensive study of fracture evolution of brittle rock containing an inverted U-shaped cavity under uniaxial compression. Computers and Geotechnics, 116, 103219. https://doi.org/10.1016/j.compgeo.2019.103219

[12] Wu, H., Zhao, G. Y., & Liang, W. Z. (2019). Mechanical response and fracture behavior of brittle rocks containing two inverted U-shaped holes under uniaxial loading. Applied Sciences, 9(24), 5327. https://doi.org/10.3390/app9245327

[13] Cao, R. H., Cao, P., & Lin, H., et al. (2018). Mechanical behavior of an opening in a jointed rock-like specimen under uniaxial loading: Experimental studies and particle mechanics approach. Archives of Civil and Mechanical Engineering, 18(1), 198-214. https://doi.org/10.1016/j.acme.2017.06.010

[14] Huang, Y. H., Yang, S. Q., Hall, M. R., et al. (2018). Experimental study on uniaxial mechanical properties and crack propagation in sandstone containing a single oval cavity. Archives of Civil and Mechanical Engineering, 18, 1359-1373. https://doi.org/10.1016/j.acme.2018.04.005

[15] Yang, S. Q., Tian, W. L., Huang, Y. H., et al. (2018). Experimental and discrete element modeling on cracking behavior of sandstone containing a single oval flaw under uniaxial compression. Engineering Fracture Mechanics, 194, 154-174. https://doi.org/10.1016/j.engfracmech.2018.03.003

[16] Yang, S. Q., Huang, Y. H., Tian, W. L., et al. (2017). An experimental investigation on strength, deformation and crack evolution behavior of sandstone containing two oval flaws under uniaxial compression. Engineering Geology, 217, 35-48. https://doi.org/10.1016/j.enggeo.2016.12.004

[17] Yang, S. Q., Yin, P. F., Zhang, Y. C., et al. (2019). Failure behavior and crack evolution mechanism of a non-persistent jointed rock mass containing a circular hole. International Journal of Rock Mechanics and Mining Sciences, 114, 101-121. https://doi.org/10.1016/j.ijrmms.2018.12.017

[18] Liu, J. P., Li, Y. H., Xu, S. D., et al. (2015). Moment tensor analysis of acoustic emission for cracking mechanisms in rock with a pre-cut circular hole under uniaxial compression. Engineering Fracture Mechanics, 135, 206-218. https://doi.org/10.1016/j.engfracmech.2015.01.006

[19] Fan, X., Chen, R., Lin, H., et al. (2018). Cracking and failure in rock specimen containing combined flaw and hole under uniaxial compression. Advances in Civil Engineering, 2018, 9818250. https://doi.org/10.1155/2018/9818250

[20] Zhu, W. C., Liu, J., Tang, C. A., et al. (2005). Simulation of progressive fracturing processes around underground excavations under biaxial compression. Tunnelling and Underground Space Technology, 20(3), 231-247. https://doi.org/10.1016/j.tust.2004.08.008

[21] Zhao, X. D., Zhang, H. X., & Zhu, W. C. (2014). Fracture evolution around pre-existing cylindrical cavities in brittle rocks under uniaxial compression. Transactions of Nonferrous Metals Society of China, 24(3), 806-815. https://doi.org/10.1016/S1003-6326(14)63129-0

[22] Zhao, R., Tao, M., Zhao, H. T., et al. (2020). Dynamics fracture characteristics of cylindrically-bored granodiorite rocks under different hole size and initial stress state. Theoretical and Applied Fracture Mechanics, 109, 102702. https://doi.org/10.1016/j.tafmec.2020.102702

[23] Wu, J. H., Zong, Q., & Xu, Y. (2020). Experimental study of the dynamic tensile mechanical properties of a coal sandstone disc with a central hole. Advances in Civil Engineering, 2020, 8851575. https://doi.org/10.1155/2020/8851575

[24] Hudson, J. A. (1969). Tensile strength and the ring test. International Journal of Rock Mechanics and Mining Sciences & Geomechanics Abstracts, 6(1), 91-97. https://doi.org/10.1016/0148-9062(69)90029-1

[25] Inglis, C. E. (1913). Stresses in a plate due to the presence of cracks and sharp corners. Transactions of the Institution of Naval Architects, 55, 219-241. https://doi.org/10.1016/S0033-8978(13)80023-5